Temporal Structure of the Southern Oscillation as Revealed by Waveform and Wavelet Analysis

Bin Wang and Yan Wang

Department of Meteorology, School of Ocean and Earth Science and Technology, University of Hawaii at Manoa, Honolulu, Hawaii

(Manuscript received 20 April 1995, in final form 3 January 1996)

ABSTRACT

Wavelet transforms (WLT) and waveform transforms (WFT) are effective tools that reveal temporal structure of nonstationary time series. The authors discuss principles and practical aspects of their geophysical applications. The WLT can display variance as a continuous function of time and frequency, but the frequency (time) locality reduces at the high (low) frequency bands. The WFT, on the other hand, provides a sharp view of the locality in both time and frequency, but presents variance by discrete base functions. The two techniques are complementary. The authors use both Morlet WLT and Gabor WFT to analyze temporal structure of the Southern Oscillation (SO).

The principal period of the SO has experienced two rapid changes since 1872, one in the early 1910s and the other in the mid-1960s. The dominant period was 3–4 years in the earliest four decades (1872–1910), 5–7 years in the ensuing five decades (1911–1960, except the 1920s), and about 5 years in the last two decades (1970–1992). The SO also exhibits noticeable amplitude changes. It was most energetic during two periods: 1872–1892 and 1970–1992, but powerless during the 1920s, 1930s, and 1960s. The powerless period is dominated by quasi-biennial oscillation. Excessively strong cold phases of the El Niño–Southern Oscillation cycle enhance annual variation of SST in the equatorial eastern and central Pacific. The enhancement, however, appears to be modulated by an interdecadal variation.

1. Introduction

The Southern Oscillation (SO), in common with many other geophysical phenomena, is nonstationary. Troup (1965) first noticed the apparent lack of SO stationarity in the first half of the *twentieth century*. Based on a comparison of the six strongest El Niño after 1950, Wang (1995) showed that the onset of El Niño experienced an abrupt change in the late 1970s. The change of onset characteristics is attributed to a sudden variation in the background state, which is associated with a conspicuous global warming and deepening of the Aleutian Low in the North Pacific as documented by Nitta and Yamada (1989) and Trenberth (1990).

Previous studies have noted and documented two major SO elements: quasi-biennial and low-frequency components (e.g., Trenberth 1976; Meehl 1987; Rasmusson et al. 1990; Yasunari 1990; Barnett 1991), but the relationship between the two remains to be clarified. It has been recognized that the interaction between SO and the annual cycle is crucial for understanding and predicting El Niño–Southern Oscillation (ENSO) (Philander and Rasmusson 1985). The SO persistence depends on the annual cycle (Trenberth and Shea 1987;

Webster and Young 1992), as does the evolution of El Niño (Wyrtki 1975; Rasmusson and Carpenter 1982). On the other hand, the strength of the annual cycle appears to be regulated by the ENSO cycle (Gu and Philander 1995). The physical causes of the interaction is a focus of recent studies.

The spatial structure of the ENSO has been well documented (e.g., Rasmusson and Carpenter 1982; Deser and Wallace 1990; Chao and Philander 1993). Its temporal structure, however, has been less well documented because of the limited length of observation and lack of adequate methodology. The Fourier transform (FT), including spectral and cross-spectral analyses, has been a major tool for investigation of temporal structure of the SO (e.g., Trenberth 1976; Trenberth and Shea 1987). It maps a signal from time to frequency domain, providing a time-mean power spectrum. As such, it fails to reveal possible changes of the oscillation characteristics with time.

Efforts have been made to overcome the drawback of Fourier analysis by constructing a "window" in the time domain so that local spectral information can be identified. Gabor (1946) first introduced a Gaussian window with predefined width. With a fixed window width, however, the so-called *Window Fourier Transform* is not suitable for detecting a signal that possesses a wide range of timescales.

A newly developed technique called *wavelet transform* (WLT) relates window width with the frequency

Corresponding author address: Dr. Bin Wang, Department of Meteorology, University of Hawaii at Manoa, 2525 Correa Road, Honolulu, HI 96822.

of base function, forming a flexible time window to overcome the weakness of the Window Fourier Transform. The one-dimensional continuous wavelet transform was first introduced by Morlet (1982) and Grossman and Morlet (1984). The WLT has been recently applied to oceanic and meteorological analyses of various fields: daily pressure (Serrano et al. 1992), rainfall (Kumar et al. 1993), dispersion of Yanai waves (Meyers et al. 1993), satellite infrared radiance (Weng and Lau 1994), and sea surface temperature (Gu and Philander 1995).

A serious problem arises when the window width is connected with frequency. Once the window widens, local information would be diluted on a broader base and the time locality is degenerated. When a signal involves components that vary in wide ranges of time and frequency, more flexible bases are desirable. Mallat and Zhang (1993) have recently advanced a new transform called *waveform transform* (WFT) to meet this need. The time–frequency properties of the WFT bases are fully adaptable to local structures of a signal.

We first present a brief survey of the WLT and WFT and compare their advantages and weaknesses through idealized examples. We then employ both approaches to reveal nonstationarities of the SST variation in the equatorial Pacific and the SO. Specific attention is paid to the interdecadal changes in the SO and the relationship between the annual cycle and ENSO and the relationship between the two components (the quasi biennial and low frequency) of the ENSO.

2. The wavelet and waveform transform

Consider a continuous nonstationary time series $f(t)$. To decode this signal in a frequency-time domain, one needs a family of base functions that are sufficiently localized in both time and frequency.

a. Wavelet transform

Morlet (1982) designed the following flexible window base functions:

$$G_L(t) = \frac{1}{(s)^{1/2}} g\left(\frac{t-u}{s}\right) e^{i(\xi_0/s)t}, \qquad (1)$$

where $g(t)$ is a Gaussian function for Morlet wavelet, u is a translation parameter shifting the window along the time axis, and s is called the dilation parameter controlling the window width and the oscillation period of the base function within the window. Parameter ξ_0 equals $\pi(2/\ln 2)^{1/2}$ in order to satisfy the admissibility condition (Farge 1992). In Fourier space, this family of functions is expressed by

$$\hat{G}_L(\omega) = \int_{-\infty}^{+\infty} G_L(t) e^{-i\omega t} dt \qquad (2)$$

$$= \sqrt{s} \hat{g}(s\omega - \xi_0) e^{-i(\omega - \xi_0/s)u}, \qquad (3)$$

where $\hat{g}$ denotes the Fourier transform of g. Because the window width and the frequency of base function are adjustable, at any given time the high-frequency structure can be detected by decreasing s (narrowing the window), while the low-frequency structure can be explored by increasing s (widening the window).

The inner product of a signal with wavelets is defined as its WLT:

$$(\mathcal{W}_{G_L} f)(u, s) = \langle f(t), G_L(t) \rangle \qquad (4)$$

$$= \int_{-\infty}^{+\infty} f(t) \bar{G}_L(t) dt, \qquad (5)$$

where $\bar{G}_L(t)$ is the complex conjugate of $G_L(t)$. Physically, the coefficients of WLT express energy densities (Farge 1992). With u as abscissa and ξ or ξ_0/s as ordinate, the WLT simply maps a signal into a time-frequency domain. We note, however, transforming low-frequency variations in a signal requires a wide time window. The signals would then be diluted in a large time base and the time locality thus reduced: One cannot precisely determine the time at which the low-frequency oscillation is centered. On the other hand, when detecting high-frequency variations, the width of frequency window must be wide. As such, the frequency locality is degraded in the high-frequency band. In addition, WLT cannot adequately estimate energy spectrum at the two ends of the time series due to "end effect."

b. Waveform transform

To overcome the weakness of the WLT, a new method, known as waveform transform, was developed by Mallat and Zhang (1993). It uses three parameters to provide a more flexible window: a translation parameter u_n; a frequency parameter, ξ_n, which determines the oscillation frequency in the window; and a scaling parameter, s_n, which controls the window width. The base function $g(t)$ is decomposed into countable window functions, which have the form

$$G_{\gamma_n}(t) = \frac{1}{(s_n)^{1/2}} g\left(\frac{t-u_n}{s_n}\right) e^{i\xi_n t}, \qquad (6)$$

where $\gamma_n = (s_n, u_n, \xi_n)$ and $n \in N$. The $G_{\gamma_n}(t)$ is referred to as *Waveform*. Because the waveforms involve three parameters, a signal cannot be mapped into a time-frequency domain by simply taking an inner product of the signal and waveforms. Instead, by carefully selecting G_{γ_n} and the weights among them, it is possible to express a signal $f(t)$ as

$$f(t) = \sum_{n=-\infty}^{+\infty} a_n G_{\gamma_n}(t). \qquad (7)$$

The weight coefficients a_n represent local characters and contents of frequency in the signal. After deter-

mination of the scaling (s_n), modulation (ξ_n), and translation (u_n) parameters, and the coefficients a_n based on local properties of the signal, one can plot the resultant waveforms in a time–frequency plane using the Winger distribution (Mallat and Zhang 1993). If $g(t)$ is a Gaussian window such as

$$g(t) = 2^{1/4} e^{-\pi t^2}, \tag{8}$$

then the Winger distribution $\mathcal{W}g(t, \omega)$ is

$$\mathcal{W}g(t, \omega) = 2e^{-2\pi[t^2+(w/2\pi)^2]}. \tag{9}$$

The WFT can then be defined by

$$(\mathcal{W}_{G_r}f)(t, \omega) = \sum_{n=0}^{+\infty} |\langle R^n f, G_{\gamma_n}\rangle|^2$$

$$\times \mathcal{W}g\left(\frac{t-u}{s}, s(\omega-\xi)\right), \tag{10}$$

where $R^n f$ is the residue vector after approximating f in the direction of G_{γ_n}.

The distribution of waveforms expresses energy density as a function of time and frequency. If a single waveform element cannot precisely match local properties in a signal, the residue would be further projected onto a series of subwaveforms until energy conservation or a threshold of iteration is satisfied. The above procedure can be viewed as a suitable descriptive metaphor. The signal is treated as a coded book, whereas series of base functions constitute a dictionary. One needs to select a word explanation (waveform) from the dictionary to decode the book in order to read it.

The key of this procedure is to select adaptive waveforms over base vectors in a dictionary to best match local properties of $f(t)$ so that Eq. (7) is established. An algorithm, called *Matching Pursuit,* is developed to perform this adaptive decomposition. For more details of the procedure, readers are referred to Mallat and Zhang (1993). The Matching Pursuit method, rather than matching the base vector G_{γ_n} to the signal f, iteratively subdecomposes the residue Rf by projecting it onto countable base vectors in the dictionary that best matches Rf. This transform is based on an energy conservation equation:

$$\|f\|^2 \equiv \int_{-\infty}^{+\infty} |f(t)|^2 dt \tag{11}$$

$$= \sum_{n=0}^{m-1} |\langle R^n f, G_{\gamma_n}\rangle|^2 + \|R^m f\|^2. \tag{12}$$

Since the algorithm can be modified by selecting several vectors from the base dictionary at each iteration and by projecting the residue over the space generated by these vectors, $R^m f$ decreases when m increases. Eventually one can obtain a complete dictionary, when $|R^m f\| = 0$. The dictionary constructed using Gaussian functions in waveform transform is called the *Gabor*

dictionary. Each waveform selected by Matching Pursuit is an elongated Gaussian blob, which is represented by a Winger distribution in a time–frequency plane. To give a more precise description of frequency contents in a signal, Dirac base and Fourier base are also supplemented into the Gabor dictionary.

c. Reconstruction and quasi-orthogonal frame

The energy is conserved after WLT. For WFT, energy conservation is our criterion to stop the iteration of algorithm. The decomposed signal can be reconstructed completely from decomposition coefficients. For WLT, the reconstruction formula is

$$f(t) = \frac{1}{C_g} \iint (\mathcal{W}_{G_L}f)(u, s) G_L(t) \frac{duds}{s^2}, \tag{13}$$

where

$$C_g = \int \frac{|\hat{g}(\omega)|^2}{\omega} d\omega. \tag{14}$$

In WFT, the formula of reconstruction reads

$$f(t) = \sum_{n=0}^{+\infty} \langle R^n f, G_{\gamma_n}\rangle G_{\gamma_n}, \tag{15}$$

where $R^n f$ is the nth order residue of Matching Pursuit.

The decomposition and the reconstruction work as if the base functions in the two transforms constitute a complete orthogonal set in a Hilbert space. For continuous WLT, the bases are redundant and signal is oversampled in the transform. For discrete WFT, the dictionary is also redundant. Two benefits can be obtain from the redundancy in the signal reconstruction. First, there exist many different reconstruction formulas. One can find a very simple formula to recover the signal from its decomposition coefficients (Farge 1992; Goupillaud et al. 1984). Second, one can select a subset called frame from Hilbert space to constitute an approximately orthogonal base so that the efficiency of decomposition and construction can be improved. Since this frame in the phase space is approximately orthogonal, it is named a *quasi-orthogonal* frame. In WLT, the base for decomposition is selected on the grids ($nu_0 s_0^m$, s_0^m) in the phase space. In WFT the index set is composed of all $\gamma = (2^j, p2^{j-1}, k\pi/2^j)$ with $0 < j < \log_2 N$, $0 \leq p < N2^{-j+1}$, and $0 \leq k2^{j+1}$. Here, N expresses the total number of sampling points.

The concept of quasi-orthogonal frame theoretically expands the concept of orthogonality. It implies that one can use the coefficients at some special points to reconstruct the signal. The number of selected points are flexible, depending on the precision requirements of users. For WFT, finite vectors based on the quasi-orthogonal frame are included in the dictionary.
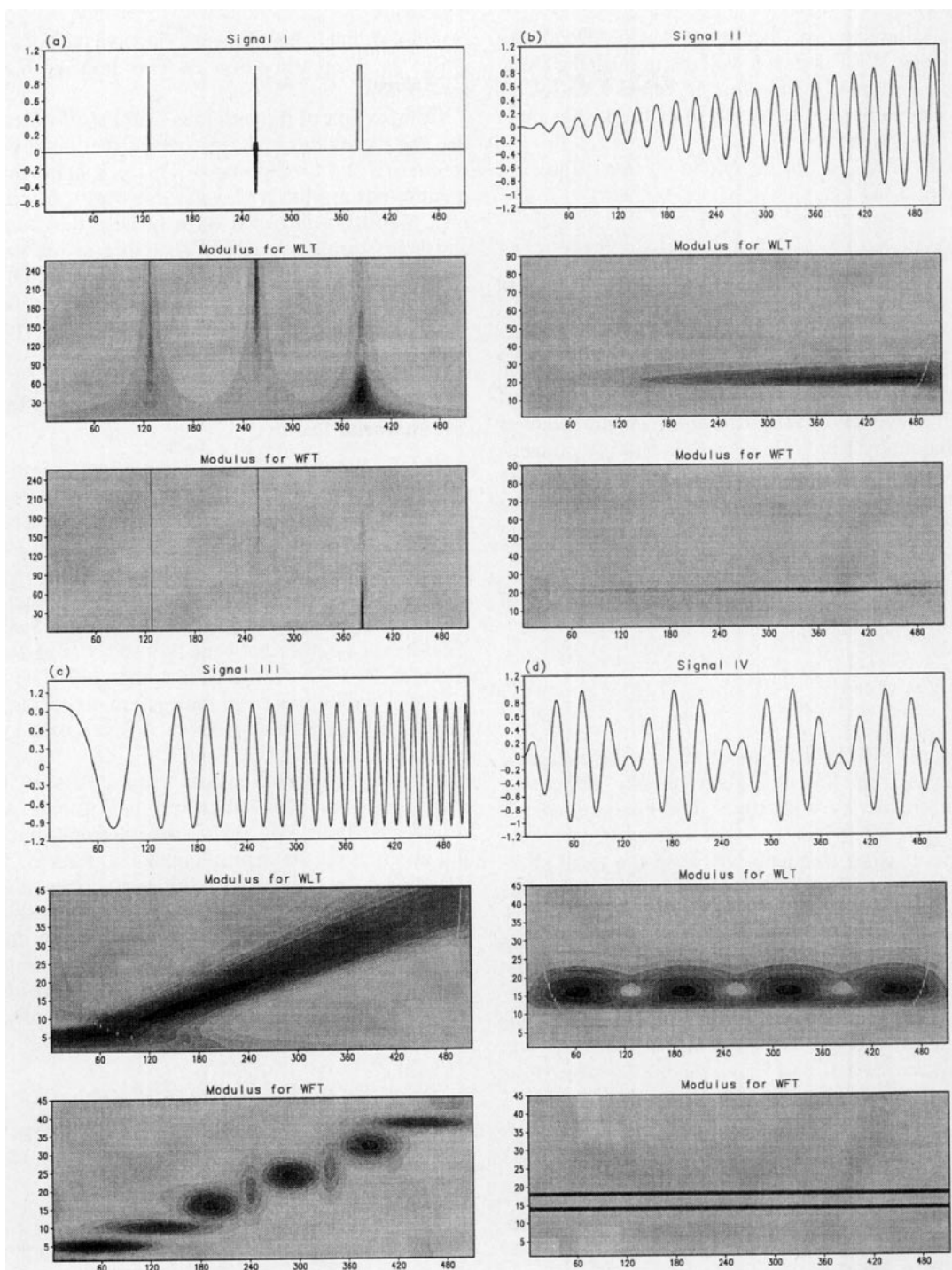
FIG. 1. The modulus of wavelet transform and waveform transform as function of time (abscissa) and frequency (ordinate) for signal I (a), II (b), III (c), and IV (d). The unit for time is arbitrary. The frequency is expressed in terms of wavenumber with a unit of $1/T$, where T is the total length of the time series.

d. Examples

Four types of signal were designed to illustrate the properties of the two transformations.

Signal I consists of a Dirac pulse (left), a very short-life vibration (middle), and a rectangular pulse (right) (Fig. 1a). An arbitrary nondimensional time unit is used. The large time base of WLT in low-frequency

leads to a failure in time locality at the low-frequency band. Besides, WLT does not well distinguish the Dirac pulse from a short-life vibration. In contrast, the WFT provides excellent time locality and distinguishes three types of pulse clearly.

Signal II (Fig. 1b) is generated by the following function:

$$f(t) = \frac{t}{512} \cos\left(\frac{2\pi}{24} t\right) \quad t \in [0, 512], \quad (16)$$

which represents an oscillation with a constant frequency and an amplitude that increases linearly with time. In both transforms, energy density increases with time, correctly reflecting the increasing amplitude of the signal. However, in WLT, the energy is diluted over a wide frequency band, whereas it is sharply concentrated in a narrow frequency band in WFT. The energy is spread to a wide frequency band in WLT near the end of the signal. Some subwaveforms also appear near the end to satisfy local character of the signal in WFT.

Signal III (Fig. 1c) represents an oscillation with a constant amplitude and a frequency increasing with time:

$$f(t) = \cos\left(\frac{2\pi}{24} \frac{t^2}{T}\right), \quad t \in [1, 512]. \quad (17)$$

Here T equals 512. In WLT modulus, a wide energetic band extends from low to high frequency, indicating change of frequency with time. The energetic band, however, spreads wider and the intensity decreases with the increasing frequency because the local character of signal is diluted when WLT depicts high-frequency variation. Meanwhile, the WLT spreads energy in a larger time window at the low-frequency band. The time locality is, therefore, destroyed there. In WFT, the detected frequency change is sharper but is discontinuous due to the discretized base functions. Complementary subwaveforms are observed in the time–frequency plane.

The signal of IV (Fig. 1d) is constructed by

$$f(t) = \sin\left(\frac{2\pi}{32} t\right) \sin\left(\frac{2\pi}{256} t\right) \quad t \in [1, 512]. \quad (18)$$

The signal contains an amplitude oscillation with a period of 256 units and a basic carrier with a period of 32 units. This signal can be recast into

$$f(t) = 0.5 \times \left[\cos\left(\frac{2\pi}{28.44} t\right) - \cos\left(\frac{2\pi}{36.57} t\right) \right]$$
$$t \in [1, 512]. \quad (19)$$

The WLT shows amplitude oscillation clearly but the carrier frequency is smeared. On the other hand, the WFT is capable of determining precisely the two frequencies of Fourier harmonics involved Eq. (19). The

original signal is interpreted as a wave packet by WLT, while as a superposition of two Fourier harmonics by WFT.

Comparison of the previous four cases indicates that the WFT provides a sharp view of the locality in both frequency and time domain. This is a major improvement over the Morlet wavelet transform. But the complex algorithm is based on a quasi-orthogonal frame and leads to a discrete cell structure in the time–frequency spectrum. The WLT captures scale characteristics of signals but lost frequency locality at the high-frequency band and time locality at the low-frequency band.

3. Temporal structure of SST variations in the equatorial Pacific

The SST data used here are derived from monthly mean COADS (Comprehensive Ocean–Atmosphere Data Sets) of MSTs (Monthly Summaries Trimmed) for the period of January 1950–December 1992. To ensure sufficient data density for a reliable estimation of monthly mean SST, we selected two rectangular areas, each covering an area of 10° lat × 15° long. They straddle the equator between 5°S and 5°N and are centered at 87.5°W (80°–95°W) and 162.5°W (155°–170°W), which represent the eastern and central equatorial Pacific Ocean, respectively. Since both locations are collocated with ship routes, the data density is the best in the equatorial eastern-central Pacific. The averaged monthly observation numbers for the selected period are about 300 at the eastern equatorial Pacific and about 50 at the central equatorial Pacific. The observational frequencies in the two boxes are fairly steady after the late 1950s (Fig. 2). The monthly mean SSTs for each location were computed from data-density weighted averages from each 2° lat × 2° long grids. Further data quality control was performed to assure temporal and spatial consistencies. Details of the data processing are discussed by Wang (1995).

a. SST in the eastern equatorial Pacific

The variation of monthly mean SST in the eastern equatorial Pacific is dominated by the annual cycle,
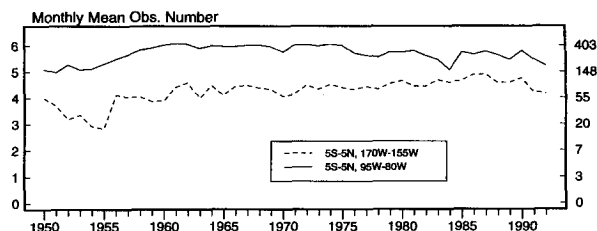

FIG. 2. Monthly observation number in the eastern and central Pacific boxes defined in the figure legend. The monthly observation numbers are averaged over each calendar year. The right (left) ordinate is actual (natural logarithm of) observation numbers.

which is, however, modulated by the El Niño–La Niña cycle (Fig. 3a). The SST variance is displayed as a function of period and time by the modulus of WLT (Fig. 3b) and WFT (Fig. 3c). Concentration of energy on two primary timescales—the annual and ENSO— is obvious. The amplitude of the annual cycle and both

the amplitude and frequency of the ENSO cycle change with time, indicating their nonstationarity.

On the annual timescale, the wavelet modulus shows a broad energetic band due to dilution of energy to adjacent frequencies. This is partially caused by the use of low-resolution (monthly mean) data. However, the
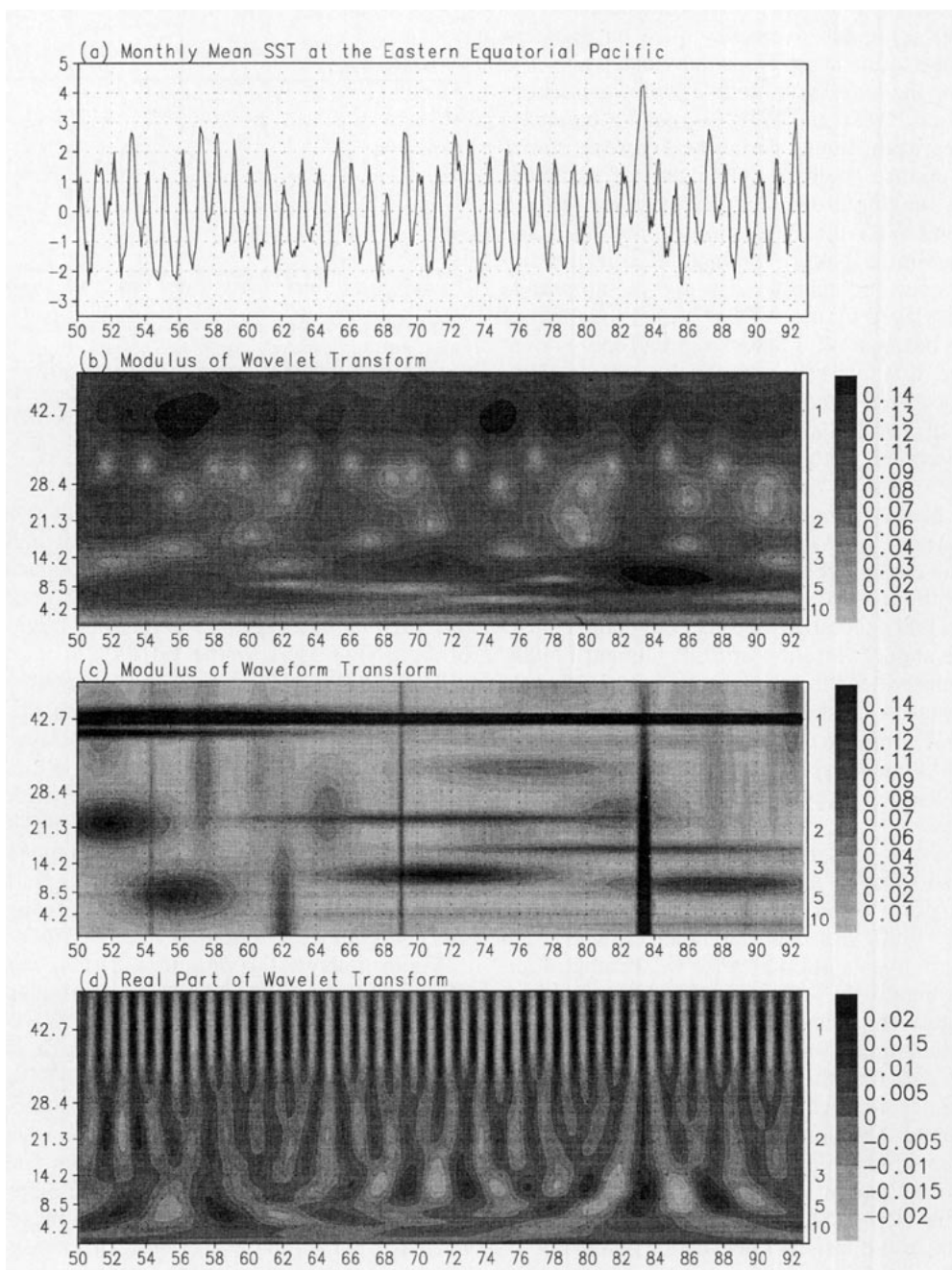

FIG. 3. (a) Monthly mean SST anomaly (in units of °C) with respect to annual mean (25.0°C) at the equatorial eastern Pacific (5°S–5°N, 95°–80°W) and the corresponding time–frequency decomposition: (b) modulus of wavelet transform (WLT), (c) modulus of waveform transform, and (d) the real part of the WLT. The abscissas are time marching forward. The left ordinates in (b), (c), and (d) are frequency (wavenumber), whereas the right ordinates denote period in units of year. Shading represents different energy density.

smeared view of the annual cycle is also associated with the intrinsic weakness of WLT: the decrease of frequency locality toward high-frequency end. In this regard, WFT offers an improved frequency locality of the energy spectrum. In waveform modulus (Fig. 3c), the energy is concentrated in a narrow frequency band, providing a sharp view of annual cycle. Note, however, that the wavelet modulus discloses visible fluctuations in the amplitude of the annual cycle, whereas the waveform modulus is unable to display such an apparent modulation due to the sharp frequency locality.

To examine the amplitude modulation of annual cycle, we use both WLT and WFT to make a bandpass filtering to segregate annual variation. Figure 4a shows the annual variance (defined as the sum of variances with periods ranging from 8 to 15 months) derived from WLT and WFT filters. Obviously, the WLT and WFT yield a similar pattern of fluctuation in the amplitude. However, the annual mean and the amplitude variability displayed by the WFT is higher than that of WLT. This is because WLT tends to spread energy over a wider range. It is interesting that major enhanced annual cycles occurred in both analyses are found during the periods of 1955–1956, 1970–1971, and 1974–1975, which concur with the three strongest La Niña episodes (1956, 1970–71, and 1974–75) (Fig. 4b). Other minor peaks in annual modulus shown by WLT or WFT alone are less faithful indicators of the enhanced annual cycle, although most of them tend to be concurrent with La Niña episodes or cold phases of SO. This suggests that excessively strong cold phases of SO may enhance annual variation of SST. Gu and Philander (1995) interpreted the enhancement of annual cycle being associated with shoaling of thermocline during La Niña, which reinforces the effect of upwelling in modulation of annual cycle of SST. Note also that the amplitude of the annual cycle decreases during most El Niño episodes.

The degree of the influence of ENSO on the annual cycle appears to vary on a longer timescale. The impact is very clear prior to the late 1970s, but is much less evident after 1980. For instance, the 1982–83 and 1986–87 warm events did not cause weakening of annual cycle, whereas the strong 1988–1989 cold event only moderately enhanced the annual cycle.

On the interannual timescale, the WLT modulus (Fig. 3b) reveals that the principal oscillation period varies with time, although the energy tends to amass in a 3–6-year band. The dominant oscillation period was about 6 years in the 1950s and the early 1960s. It abruptly shifted to about 2 years in the middle 1960s. Thereafter, the oscillation period gradually increased to about 5 years in the last two decades. The change of oscillation period is confirmed, and perhaps more clearly demonstrated, by the WFT modulus. The latter not only exhibits a better frequency separation but also a sharper temporal locality. The change in principal oscillation period is seen from the discontinuous zon-
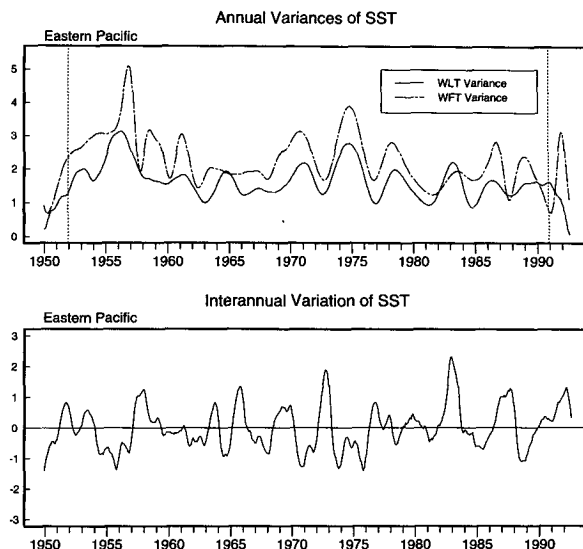

FIG. 4. The annual variance derived from wavelet and waveform transforms (upper panel), and the SST index defined by five-month running mean of the monthly mean SST anomalies at the equatorial eastern Pacific (5°S–5°N, 95°–80°W) (lower panel). Dotted lines indicate the regions affected by the "end effect" of WLT.

ally elongated energetic cells on the waveform modulus plane (Fig. 3c). The gross agreement between WLT and WFT moduli is evident. The elongated energetic cells along the time axis in the WFT modulus plane roughly coincide with the periods of large amplitudes of the ENSO signal in the WLT.

There is also an indication of concentration of energy on a quasi-biennial timescale in both the WLT and WFT analyses. The quasi-biennial oscillation exhibits a considerable amplitude modulation on a decadal timescale. It is relatively strong in the periods of 1950–1953, 1963–1967, 1972–1976, and 1981–84 as seen from Fig. 3b. The WFT modulus suggests a similar conclusion except that the two vigorous periods, 1963–67 and 1972–76, are represented by a single continuous energetic cell, spanning 1962 to 1983.

Figure 5 shows the variances in quasi-biennial (1.6–2.5 year) and ENSO (3–7 year) timescales derived by averaging the results obtained from WLT and WFT. The amplitude of the quasi-biennial cycle is sometimes out of phase with the amplitude of ENSO cycle. Such examples are found around 1953 and 1965.

The real part of the WLT (Fig. 3d) depicts actual SST fluctuation as a function of time and frequency (period). Warm episodes are generally recognized from the convergence of the constant phase line, which results in an in-phase accretion of energy on a wide frequency range. For instance, anomalies in different frequency bands or in a wide frequency range are nearly in phase during 1951 and 1953 (2 and 6–7 years), 1957–1958 (1.5–10 years), 1965 (1.5–7 years), 1972 (1.5–10 years), 1982–1983 (1.5–15
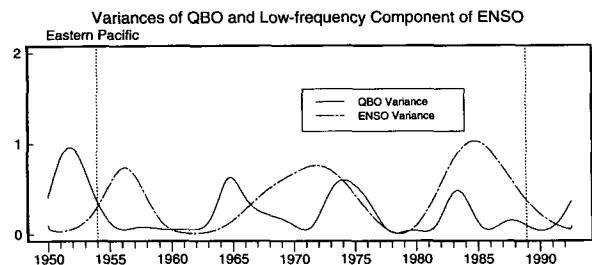
Variances of QBO and Low-frequency Component of ENSO
Eastern Pacific

FIG. 5. The variances of the QBO (2–3 years) and low-frequency (3–7 years) components of ENSO at the eastern equatorial Pacific (5°S–5°N, 95°–80°W). They are obtained by averaging those derived from WLT and WFT filters. The unit for ordinate is °C². Dotted lines indicate regions possibly influenced by the "end effects" of WLT.

years), 1987 (1.5–5 years), and 1991–1992 (1.5–10 years). Since the convergence of constant phase lines generally represents a singularity, the El Niño episodes are, to certain degrees, interpreted as singularities by WLT. On the WFT modulus plane, singularities are portrayed by vertical energetic specks penetrating a wide range of frequency. The strongest 1982–83 El Niño stands out as the most prominent singularity in both the WLT and WFT interpretation.

b. SST in the central equatorial Pacific

In the central Pacific (Fig. 6a), interannual variations are so dominant that the annual cycle is hardly visible. But computation of the climatological annual cycle reveals an annual peak warming occurring in May and a peak cooling in January.

In the eastern Pacific (110°W), the annual peak cooling occurs in September or October and it is progressively later westward along the equator (Horel 1982; Wang 1994). In the central Pacific (160°W) the peak annual cooling occurs in January. The period from September to January can be viewed as an annual cold season in the equatorial eastern-central Pacific. We note that pronounced peak ENSO warming with an anomalous SST exceeding 1.5°C occurred in October 1957, October 1965, November 1972, October 1982, August 1987, and January 1992. They indicate mature phases [a terminology given by Rasmusson and Carpenter (1982)] of the six major El Niño episodes occurring in the last four decades. Major La Niña episodes with SST 1.5° below normal peaked in January 1950, December 1955, January 1971, December 1973, November 1975, and January 1989. Therefore, nearly all the mature phases of the major warm and cold episodes tend to peak in the cold season of the equatorial eastern-central Pacific from October to January. This implies that the cold season in the equatorial eastern and central Pacific favors occurrence of large-amplitude interannual fluctuation.

The dominant period of interannual SST variation varies with time, as is the case in the eastern equatorial

Pacific. This can be seen from Figs. 6b and 6c. The WLT modulus (Fig. 6b) shows a remarkably similar change of frequency to that in the eastern equatorial Pacific. A 6-yr oscillation dominates interannual variation from 1950 to 1964 and then suddenly gives way to a quasi-biennial oscillation in the mid-1960s. Starting from the late 1960s a relative steady quasi-5-yr oscillation is maintained up to 1992. The information conveyed by WFT modulus is in a general agreement with what are reflected in WLT modulus.

In the modulus plane of WFT (Fig. 6c), two pronounced Fourier harmonics can be observed. They do not appear in WLT. One is the annual cycle, which is weak but clearly identified by WFT. The other is the quasi-biennial oscillation, which consists of two harmonics with periods of about 2.2 and 2.4 years. They interfere with each other, resulting in a wave packet–like oscillation pattern with a quasi-biennial carrier and an amplitude modulation on a decadal timescale. In the real part plane (Fig. 6d), the El Niño in 1957–58, 1965, 1972, 1976–77, 1982–83, 1987, and 1991–92 appear as singularities.

4. Interdecadal variation of the Southern Oscillation

The analysis in the previous section indicates a secular SST variation on timescales longer than a decade. To further explore interdecadal variations of SO, we need sufficiently long records. The data used here consist of seasonal mean SST anomalies averaged over the equatorial eastern and central Pacific (5°S–5°N, 180–80°W) (SST index hereafter) and monthly mean Darwin sea level pressure (SLP) anomalies, both ranging from 1872 to 1995. The Darwin SLP anomalies represent fluctuations in the strength of the Walker circulation across the equatorial Pacific with high values during warm episodes and low during cold episodes. The Darwin SLP and SST index are physically coupled and both can be used as a SO index.

The SST index was derived from original COADS using the optimal averaging technique of Smith et al. (1994). Because of the inhomogeneity of the ship-by-opportunity observation and marginal data quality in some time intervals, cautions must be exercised especially when the pre-1950 SST data are used. The Darwin SLP is a more reliable index for SO because it is homogeneous and hardly suffers from missing data. The Darwin SLP data spanning from 1872 to 1881 were compiled by Allan et al. (1991), while the data after 1882 were carefully calibrated by Trenberth and Shea (1987). Wright (1984) compared several indices of SO and concluded that on annual basis the SST, Darwin SLP, rainfall, and Darwin minus Tahiti SLP are almost equivalent. To give the two indices comparable temporal resolution, the seasonal mean SST anomalies were linearly interpolated to monthly resolution. To further increase the signal-to-noise ratio, an 11-term low-pass filter suggested by Trenberth (1984)
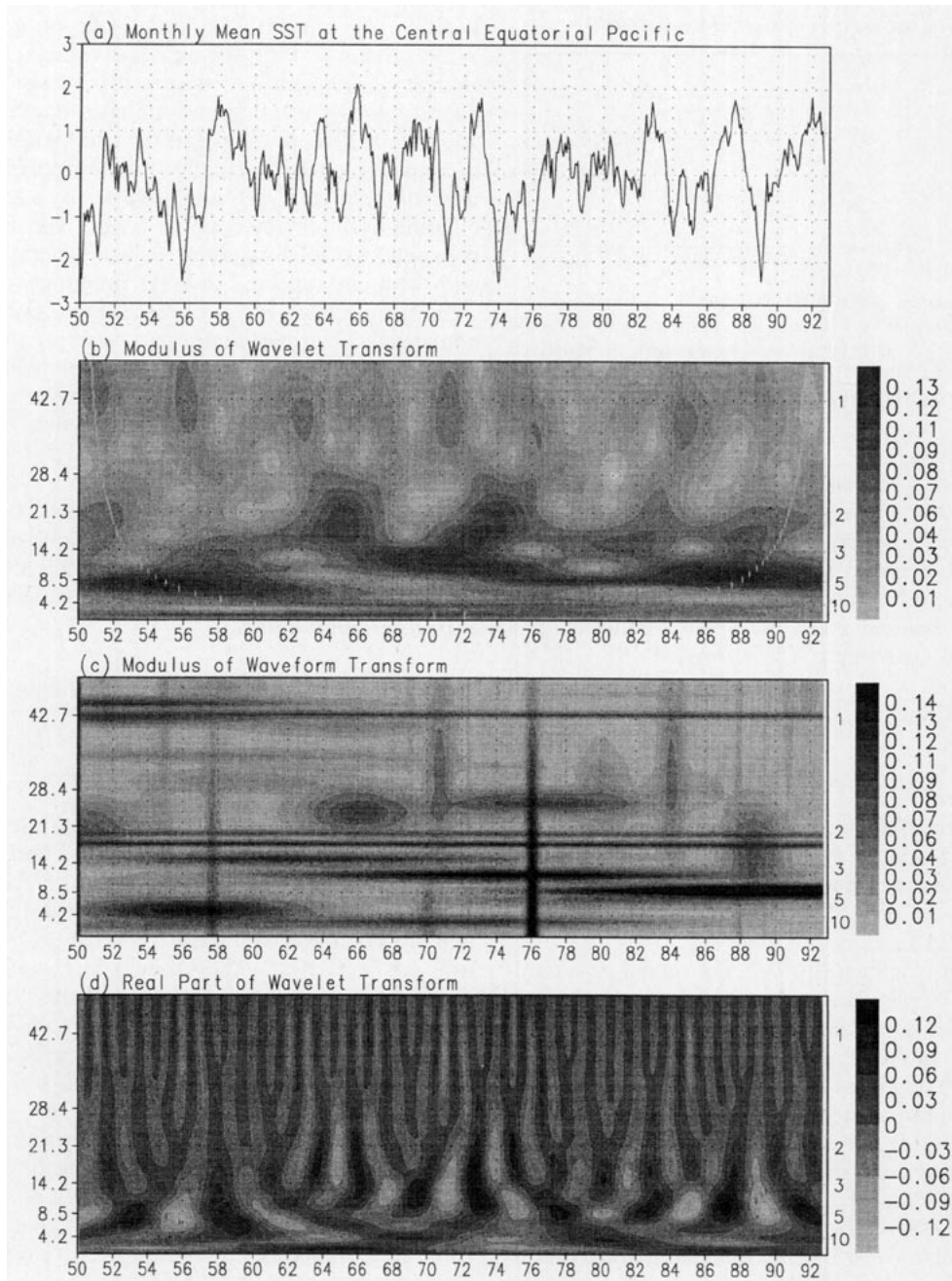
FIG. 6. As in Fig. 3 except for the SST anomalies at the central equatorial Pacific.
The annual mean SST is 27.8°C.

was applied to both indices before the WLT and WFT analysis. Comparison of the results obtained from analysis of the two indices adds confidence to our conclusions.

Figures 7 and 8a compare the moduli of WLT of the SST and Darwin SLP. In the last four decades during which the quality of the SST observation is reasonably reliable, the time–frequency spectra of the two indices are remarkably alike. They also bear great similarity to those of the eastern and central Pacific SST discussed previously. For the pre-1950 period, although the two time–frequency spectra bear some similarities, the discrepancies evidently increase backward in time. This is attributed to sparse and nonhomogeneous SST observations before 1950 (in particular in the last century), because the physical link between the two indices should be fairly steady over the years. To deduce the behavior
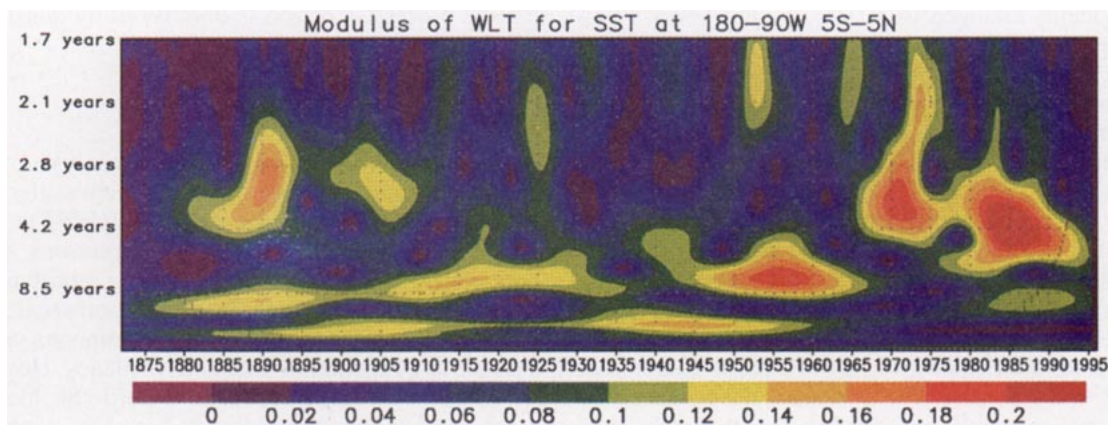
FIG. 7. The modulus of wavelet transform of 11-month weighted running mean SST anomalies averaged over equatorial eastern and central Pacific (5°S–5°N, 180–80°W). The convention is the same as in Fig. 3b.

of interdecadal variations of SO, we use Darwin SLP as an SO index.

The WLT and WFT analyses reveal that the frequency of SO evolves constantly with time in the past 124 years (1872–1995). The moduli of WLT and WFT (Figs. 8a and 8b) show similar energetic patterns. There exist obvious changes in predominant frequency of SO. The SO is characterized by a strong 4-yr oscillation during 1872–1890, then by a 3-yr oscillation during 1890–1910. In the 1910s the predominant pe-
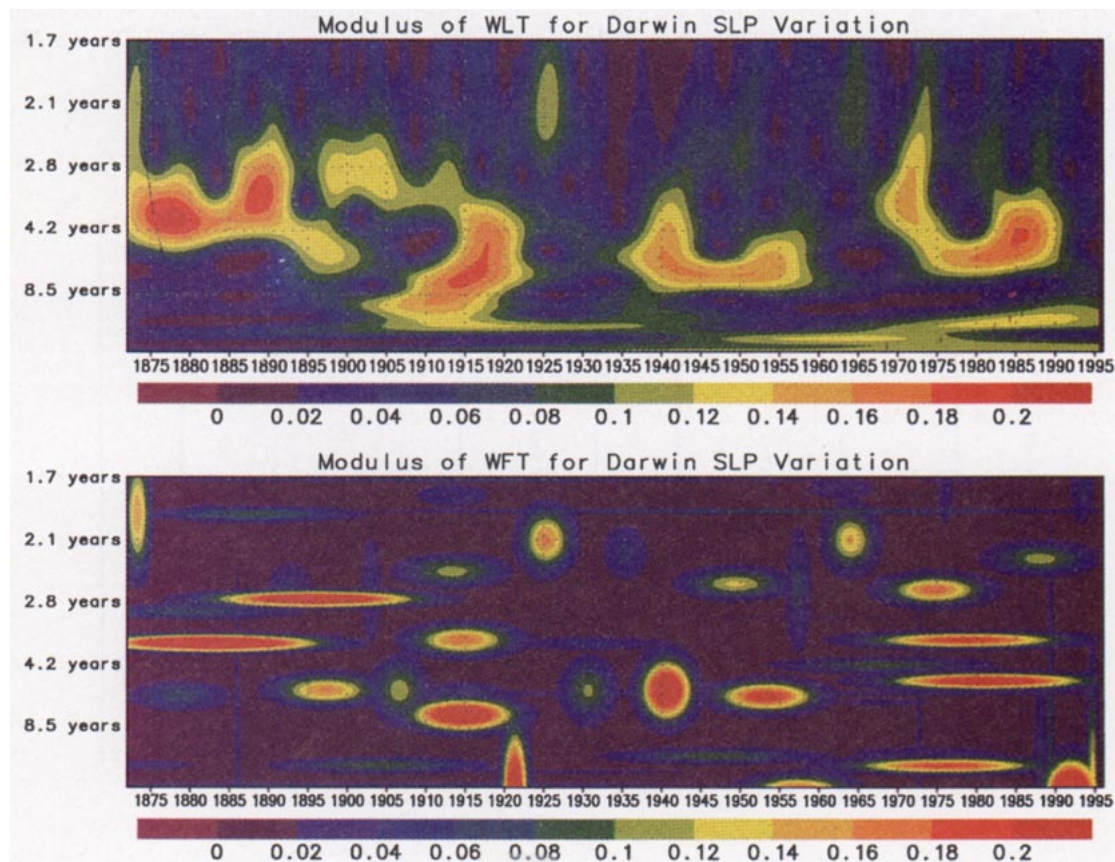

FIG. 8. The modulus of wavelet transform (a) and waveform transform (b) of the 11-month weighted running mean Darwin sea level pressure anomaly. The convention is the same as in Figs. 3b and 3c.

riod suddenly changed from 3 to about 7 years. From 1940 to 1960 the predominant oscillation period is around 5–6 years. Another abrupt alteration of oscillation period from 5–6 years to 2 years occurred in the mid-1960s. After 1971, a quasi periodicity of 4–5 years dominates.

As a result of incessant change of the primary frequency, the time mean spectrum averaged over the entire period of analysis exhibits a broad band of energy concentration ranging from 2.5–7 years in both the Fourier spectrum (Fig. 9a) and the global WFT spectrum (time-mean WFT modulus; Fig. 9b). Within this broad band, there appear to be three peaks centered at 2.8, 3.8, and 5.8 years. These frequencies, however, do not occur persistently and simultaneously. Rather, they reflect predominant frequencies for different intervals of time as revealed by WLT and WFT analyses. The high-frequency (2–3 year) component displays relatively large amplitude during three periods: 1885–1905, 1920s, and 1963–1982 (Figs. 8a,b). In general, the 2–3 yr oscillation tends to be out of phase with the 5–6 yr oscillation.

The SO amplitude also experiences marked changes in the last 124 years. There are periods during which the SO is relatively less energetic. Roughly speaking, the powerless periods include the 1920s, 1930s, and 1960s. Energetic periods are found in four intervals: 1870–1890, 1910s, 1940–1957, and 1970–1992. Note

that the powerless period is dominated by quasi-biennial oscillation.

5. Conclusions and discussion

In contrast to Fourier spectrum analysis, which yields a time mean energy spectrum, the wavelet transform (WLT) and waveform transform (WFT) can reveal temporal structure of an energy spectrum. This is particularly valuable for investigating nonstationary time series. The WLT is designed to capture scale characteristics in a signal. It provides a continuous view of variance as a function of time and frequency. However, the frequency locality reduces toward the high-frequency end and the time locality decreases toward the low-frequency end. The WFT, on the other hand, is designed to overcome the deficiency of WLT. It grants a sharp view of the locality in both time and frequency, but tends to yield a discontinuous energy distribution because of its discretized base functions.

To reveal temporal structure of the Southern Oscillation (SO), we applied Morlet wavelet transform and a waveform transform with Gabor dictionary to display time–frequency characteristics of SST variations in the equatorial eastern and central Pacific and Darwin sea level pressure variance since 1872.

The principal frequency of SO evolved continuously in the past 124 years (1872–1995). In the first two
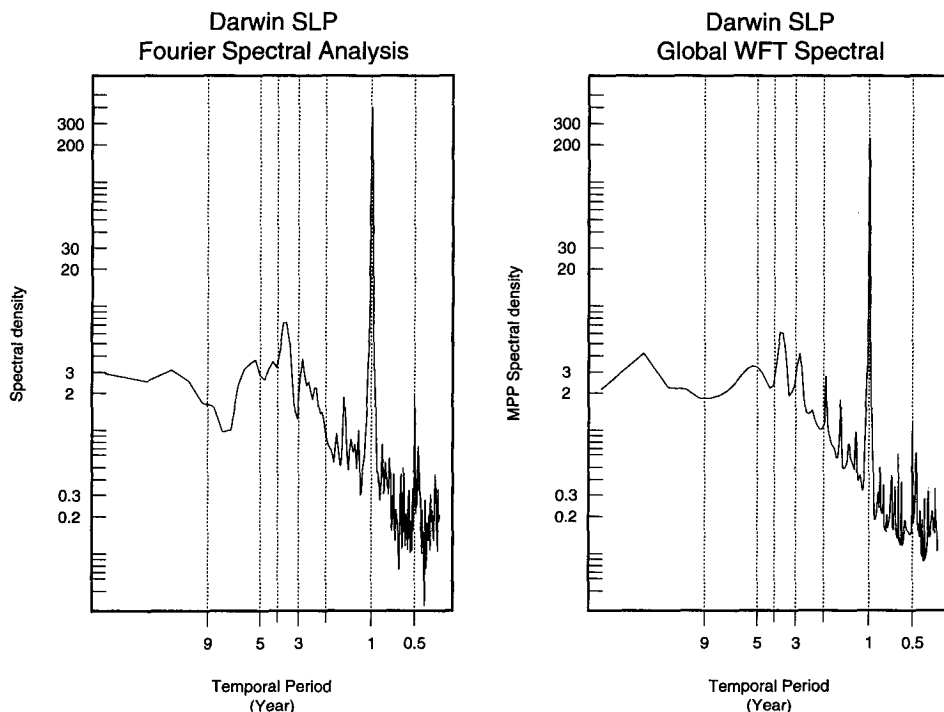
FIG. 9. Fourier spectrum (a) and global waveform transform spectrum (b) of the monthly mean Darwin sea level pressure.

decades (1872–1891), the SO is characterized by a 4-year oscillation; during 1891–1910 the primary oscillation period is about 3 years; in the ensuing five decades (roughly 1911–1960) the predominant oscillation period is around 5–7 years, although the amplitude is small during 1921–1938. In the last two decades (1972–1992), a 4–5 yr periodicity dominates. The oscillation period abruptly changed from 6 years to 2–3 years in the mid-1960s. A similar significant shift of oscillation period from 3 to 7 years occurred around 1910.

The time mean spectrum (global WFT spectrum and Fourier spectrum) shows a broad energetic band from 2.5 to 7 years, which results from alternative dominance of 2.5–3 yr, 3–4 yr, and 5–6 yr components. The 2.5–3 yr component of ENSO exhibits large amplitude during 1885–1905, 1920s, and 1963–1982. It tends to be out of phase with the low-frequency (5–6 yr) component. The lack of correlation in the amplitude of the two components suggest that the two components of ENSO may result from or involve different processes. Furthermore, their in-phase superposition could lead to excessively strong warm episodes, such as in the 1982–83 warm episode.

The amplitude of SO also exhibits noticeable fluctuations. The oscillation was very energetic during 1870–1890 and 1970–1992, and relatively energetic during the 1910s and 1940–1957. In contrast, there are two intervals during which the SO is "powerless": 1921–1938 and 1959–1969. In addition, the analysis here reveals considerable interdecadal variations in both the amplitude and frequency of SO.

The El Niño was viewed as an amplification of annual warming off the coast of Peru where peak El Niño occurs in Northern spring (Wyrtki 1975). The mature phase of the Pacific basinwide warming, however, takes place toward the end of the year (cold season) in the central Pacific (Rasmusson and Carpenter 1982). What is the exact nature of the phase-lock between ENSO and annual cycle? The present analysis indicates that both the basin-wide warming and cooling prefer to reach maxima in the cold season of the equatorial eastern and central Pacific from September to January. During the cold season of the equatorial eastern-central Pacific, the annual strengthening of the equatorial upwelling favors intensive amplification of positive or negative SST anomalies because the enhancement of the mean state upwelling makes SST anomalies amplify more vigorously.

Excessively strong cold phases of the ENSO enhance annual variation of SST. To a lesser degree, the warm phase of the ENSO tends to weaken the annual cycle. The impact of the ENSO on the annual cycle is robust during 1950–1976, but it appears to be delicate after 1977, suggesting that the regulation of the ENSO on the annual cycle may have experienced interdecadal changes. This is possibly due to the influence of the interdecadal variation of the background state, which

has changed the evolution characteristics of El Niño since the late 1970s (Wang 1995). In particular, the central Pacific peak warming in three recent warm episodes leads the peak warming in the far eastern equatorial Pacific. Change of the phase between the ENSO and annual warming may have resulted in the changes in the degree of the influence of ENSO on the annual cycle.

The present analysis revealed several important aspects of ENSO, which require better physical understanding. The interdecadal variability in principal frequency and amplitude of SO is critical to ENSO prediction. Unfortunately, its cause is unknown. The relationship between the 2–3 yr and low-frequency components of SO is also a critical issue for an improved ENSO theory and prediction. The interaction between the annual cycle and ENSO involves complex nonlinear dynamic processes and possibly has profound impacts on the aperiodicity and predictability of ENSO. All three aspects call for further investigations.

REFERENCES

Allan, R. J., N. Nicholls, P. Jones, and I. J. Butterworth, 1991: A further extension of the Tahiti-Darwin SOI, early ENSO events and Darwin pressure. *J. Climate,* **4,** 743–749.
Barnett, T. P., 1991: The interaction of multiple time scales in the tropical climate system. *J. Climate,* **4,** 269–285.
Chao, Y., and S. G. H. Philander, 1993: On the structure of the Southern Oscillation. *J. Climate,* **6,** 450–469.
Deser, C., and J. M. Wallace, 1990: Large-scale atmospheric circulation features of warm and cold episodes in the tropical Pacific. *J. Climate,* **3,** 1254–1281.
Farge, M., 1992: Wavelet transforms and their applications to turbulence. *Annu. Rev. Fluid Mech.,* **24,** 395–457.
Gabor, D., 1946: Theory of communication. *J. Inst. Electr. Eng.,* **93,** 429–457.
Goupillaud, P., A. Grossman, and J. Morlet, 1984: Cycle-octave and related transforms in seismic signal analysis. *Geoexploration,* **23,** 85–102.
Grossman, A., and J. Morlet, 1984: Decomposition of Hardy function into square integrable wavelets of constant shape. *SIAM J. Math. Anal.,* **15,** 723–736.
Gu, D., and S. G. H. Philander, 1995: Secular changes of annual and interannual variability in the Tropics during the past century. *J. Climate,* **8,** 864–876.
Horel, J., 1982: On the annual cycle of the tropical Pacific atmosphere and ocean. *Mon. Wea. Rev.,* **110,** 1863–1878.
Kumar, P., and E. Foufoula-Georgion, 1993: A new look at rainfall fluctuations and scaling properties of spatial rainfall using orthogonal wavelets. *J. Appl. Meteor.,* **32,** 209–222.
Lau, K. M., and P. Shen, 1988: Annual cycle, QBO, and Southern Oscillation in global precipitation. *J. Geophys. Res.,* **93**(D9), 10 975–10 988.

Mallat, and Zhang, 1993: Matching pursuit with time-frequency dictionaries. *IEEE Trans. Signal Process.,* **41,** 3397–3415.

Meehl, G. A., 1987: The annual cycle and interannual variability in the tropical Pacific and Indian Ocean region. *Mon. Wea. Rev.,* **115,** 27–50.

Meyers, S. D., B. G. Kelly, and J. J. O'Brien, 1993: An introduction to wavelet analysis in oceanography and meteorology: With application to the dispersion of Yanai waves. *Mon. Wea. Rev.,* **121,** 2858–2866.

Morlet, J., 1982: Wave propagation and sampling theory. *Geophys.,* **47,** 222–236.

Nitta, T., and S. Yamada, 1989: Recent warming of tropical surface temperature and its relationship to the Northern Hemisphere circulation. *J. Meteor. Soc. Japan,* **67,** 375–383.

Philander, S. G., and E. M. Rasmusson, 1985: The Southern Oscillation and El Niño. *Advances in Geophysics,* Vol. 28A, Academic Press, 197–215.

Rasmusson, E. M., and T. H. Carpenter, 1982: Variations in tropical sea surface temperature and surface wind fields associated with the Southern Oscillation/El Niño. *Mon. Wea. Rev.,* **110,** 354–384.

——, X. Wang, and C. Ropelewski, 1990: The biennial component of ENSO variability. *Proc. 21st Int. Liege Colloquium on Ocean Hydrodynamics,* Liege, Belgium,

Serrano, E., R. Compagnucci, and M. Fadio, 1992: The use of the wavelet transform for climatic estimates. *Proc. Fifth Int. Meeting on Statistical Climatology,* Toronto, ON, Canada, Amer. Meteor. Soc., 259–262.

Smith, T. M., R. W. Reyolds, and C. F. Ropelewski, 1994: Optimal averaging of seasonal surface temperatures and associated confidence intervals (1860–1989). *J. Climate,* **7,** 949–964.

Trenberth, K. E., 1976: Spatial and temporal variation of the Southern Oscillation. *Quart. J. Roy. Meteor. Soc.,* **102,** 639–654.

——, 1984: Signal versus noise in the Southern Oscillation. *Mon. Wea. Rev.,* **112,** 326–332.

——, 1990: Recent observed interdecadal climate changes in the Northern Hemisphere. *Bull. Amer. Meteor. Soc.,* **71,** 988–993.

——, and D. J. Shea, 1987: On the evolution of the Southern Oscillation. *Mon. Wea. Rev.,* **115,** 3078–3096.

Troup, A. J., 1965: The Southern Oscillation. *Quart. J. Roy. Meteor. Soc.,* **91,** 490–506.

Wang, B., 1994: On the annual cycle in the tropical eastern central Pacific. *J. Climate,* **7,** 1926–1942.

——, 1995: Interdecadal changes in El Niño onset in the last four decades. *J. Climate,* **8,** 267–285.

Weng, H. Y., and K. M. Lau, 1994: Wavelets, period-doubling, and time–frequency localization: Application to organization of convection over the tropical western Pacific. *J. Atmos. Sci.,* **51,** 2523–2541.

Wright, P. B., 1984: Relationship between indices of the Southern Oscillation. *Mon. Wea. Rev.,* **112,** 1913–1919.

Wyrtki, K., 1975: El Niño—The dynamic response of the equatorial Pacific Ocean to atmosphere forcing. *J. Phys. Oceanogr.,* **5,** 572–584.

Yasunari, 1990: Impact of the Indian monsoon on the coupled atmosphere/ocean system in the tropical Pacific. *Meteor. Atmos. Phys.,* **44,** 29–41.